JOURNAL OF GEOPHYSICAL RESEARCH, VOL. 100, NO. C9, PAGES 18,517–18,535, SEPTEMBER 15, 1995

Fine structure, microstructure, and vertical mixing processes in the upper ocean in the western Weddell Sea

Robin Robertson, Laurie Padman, and Murray D. Levine

College of Oceanic and Atmospheric Sciences, Oregon State University, Corvallis

Abstract. The upward flux of heat from the subsurface core of Warm Deep Water (WDW) to the perennially ice-covered sea surface over the continental slope in the western Weddell Sea is estimated using data obtained during February–June 1992 from a drifting ice station. Through the permanent pycnocline the diapycnal heat flux is estimated to be about 3 W m^{-2}, predominantly because of double-diffusive convection. There is no evidence that shear-driven mixing is important in the pycnocline. The estimated mean rate of heat transfer from the mixed layer to the ice is 1.7 W m^{-2}, although peak heat fluxes of up to 15 W m^{-2} are found during storms. It is hypothesized that isopycnal mixing along sloping intrusions also contributes to the loss of heat from the WDW in this region; however, we are unable to quantify the fluxes associated with this process. Intrusions occur intermittently throughout this experiment but are most commonly found near the boundary of the warm-core current and the shelf-modified water to the east. These heat fluxes are significantly lower than the basin-averaged value of 19 W m^{-2} (Fahrbach et al., 1994) that is required to balance the heat budget of the Weddell Gyre. Other studies suggest that shelf processes to the west of the ice station drift track and more energetic double-diffusive convection in the midgyre to the east could account for the difference between our flux estimates for this region and those based on the basin-scale heat budget.

1. Introduction

The Weddell Sea is believed to be an important component of the ocean-atmosphere system and is a significant source region for Antarctic Bottom Water (AABW) [e.g., *Gordon et al.*, 1993a, b]. The circulation is dominated by the Weddell Gyre, the structure of which is described in detail by *Orsi et al.* [1993]. The Gyre is a clockwise circulation of about 30 Sv (1 Sv = 10^6 m^3 s^{-1}) with most (~90%) of the transport being contained in a boundary current located within 500 km of the shelf break [*Fahrbach et al.*, 1994]. Water in the Gyre loses a significant amount of heat as it travels from the eastern Weddell to the northern tip of the Antarctic Peninsula. *Fahrbach et al.* [1994] estimate that the oceanic heat loss is equivalent to a flux to the atmosphere of 19 W m^{-2} when averaged over the entire Weddell Sea.

Several different mechanisms are responsible for the observed cooling. For example, *Muench et al.* [1990] found that double-diffusive fluxes in the central Gyre, away from boundaries, were comparable to the basin-scale average flux of 19 W m^{-2}. High fluxes might also occur over the broad, deep continental shelves in the southern and western Weddell Sea. Complex physical oceanographic interactions occurring on the shelves and near the shelf/slope front can contribute to the formation of AABW, including the extremely cold and dense Weddell Sea Bottom Water (WSBW) [e.g., *Carmack,* 1986; *Foster et al.*, 1987]. These processes include those due to nonlinearities in the equation of state, such as cabbeling [*Fofonoff,* 1956; *Foster,* 1972; *Foster and Carmack,* 1976a] and thermobaricity [see *Gill,* 1973]. This wide range of distinct but interacting processes implies that understanding the sensitivity of the Gyre circulation to perturbations in large-scale forcing requires first that the dominant physical processes in each region of the Weddell Sea be identified and understood.

Several physical oceanographic studies have been made in regions of the Weddell Sea where the ice cover either disappears in summer or is sufficiently thin to allow ship access. The western margin, however, is relatively inaccessible to ships because it is perennially covered with thick, second-year ice that has been advected into the region from the east. The problem of access is particularly acute in winter when the ice cover is most compact. Consequently prior to 1992, most data in this region consisted of ice drift and ice concentration measurements obtained from satellite or aircraft-borne sensors and satellite-tracked ice-mounted buoys. Even basic features of the bathymetry, such as the location of the continental slope, were inferred primarily from

Paper number 95JC01742.
0148-0227/95/95JC-01742$05.00

satellite altimetry [*LaBreque and Ghidella*, 1993]. To increase the data coverage, a manned camp, *Ice Station Weddell 1* (ISW), was established on the mobile pack ice near 52°W, 71.5°S in January 1992 by the Russian icebreaker *Akademik Federov*. A wide variety of oceanic, atmospheric, sea-ice, and biological data were collected as ISW drifted approximately northward over the central continental slope [*Gordon et al.*, 1993b]. The camp was recovered near 52°W, 66°S in early June (Figure 1). More recently (January 1993), the German research vessel Polarstern has obtained data from a cross-slope transect to the face of the Larsen Ice Shelf near 69°S [*Bathmann et al.*, 1994].

Our primary goals in this paper are to estimate the upward oceanic heat flux from the WDW to the surface in the western Weddell Sea and to identify the principal physical mechanisms responsible for this flux. Toward these goals, we summarize our observations of oceanic finestructure and microstructure at ISW and describe the processes responsible for this flux. The following section describes the data and section 3 gives an overview of the spatial and temporal variation of the upper ocean hydrography. Section 4 discusses the various processes responsible for vertical heat flux in the upper ocean. A discussion and summary are provided in section 5.

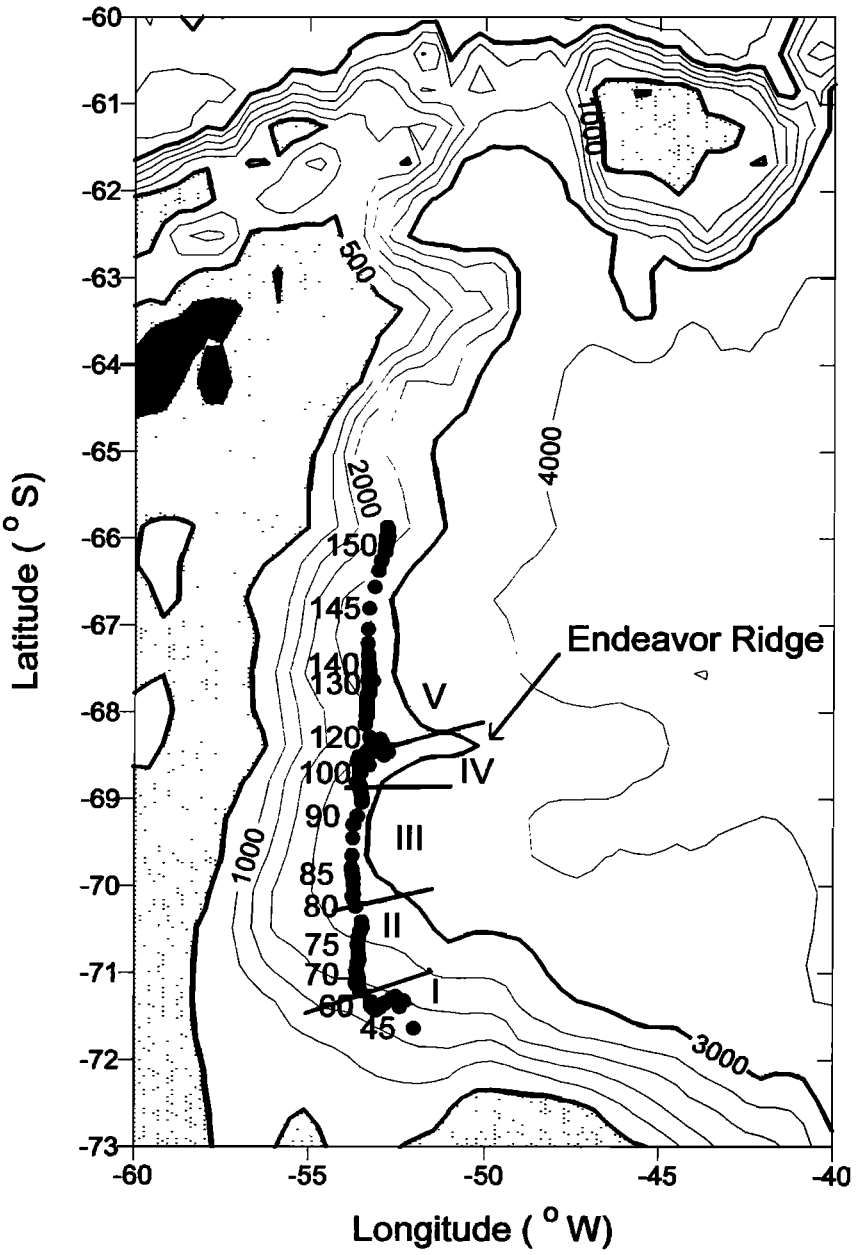

Figure 1. Drift track of Ice Station Weddell: daily positions indicated by dots. Depth contours are in meters, with depths less than 500 m being shaded. The 500- and 3000-m isobaths are shown bold. Time along drift track is in day of year. Roman numerals refer to the regimes defined in section 3.

2. The Experiment

Ice Station Weddell 1 (ISW) was established in late January 1992 on a floe of multiyear ice located over the continental slope. ISW initially drifted southwest toward shallower water, then turned northward and traveled downslope to deeper water, after which it continued northward roughly following the 3000-m isobath (Figure 1). *Gordon et al.* [1993b] review ISW and its associated measurements.

We collected approximately 700 microstructure profiles using the Rapid-Sampling Vertical Profiler (RSVP) [*Caldwell et al.*, 1985; *Padman and Dillon*, 1987, 1991] between February 26 and May 27, 1992. These dates correspond to year-days 57 and 148. Throughout this paper, time t will be given in decimal day-of-year 1992 (UTC), where $t = 1.0$ is 0000 on January 1. Most profiles reached from the surface to a depth of about 350 m, which is within the permanent pycnocline. During intensive investigations of the seasonal pycnocline, however, shallower profiles were taken, typically to 100 m. The cycling time between profiles varied from about 15 min to days. Several profiles were obtained on most days (Figure 2a), with the exception of a 10-day data gap from $t = 115$ to 124.

The RSVP is a tethered, free-fall profiler about 1.3 m long. Sensors for measuring temperature (T), conductivity (C), pressure (P), and microscale velocity shear ($u_z = \partial u/\partial z$ and $v_z = \partial v/\partial z$) are located on the nose. Each data channel was sampled at 256 Hz. The fall rate was about 0.85 m s^{-1}; therefore each profile to 350 m required about 7 min. Sensors to measure T and C were a Thermometrics FP07 thermistor and a Neil Brown Instruments Systems microconductivity cell, respectively. The conductivity required frequent recalibration, which was achieved by comparison with the closest (in time) CTD profiles obtained by Lamont Doherty Earth Observatory (LDEO). Least significant bit (lsb) resolutions of the raw 16-bit records are about 1.5×10^{-4}°C in T and 1.5×10^{-5} S m^{-1} for C. Typical rms noise levels based on measurements in nonturbulent mixed layers are comparable to the lsb resolution in T (2.1×10^{-4}°C) and an order of magnitude larger for C (1.1×10^{-4} S m^{-1}). For calculating salinity (S) and potential density (σ_θ), the mismatch between the time constants and locations of the T and C sensors was taken into account by lagging C by 0.075 m. The lag was determined by optimizing the correlation coefficient between temperature and conductivity gradients and minimizing salinity spiking. After incorporating the lag, T and C were averaged over 2 s (512 points) and used to generate values of S and σ_θ at approximately 1.7-m depth intervals. Temperatures were converted to potential temperature (θ) using S and measured P.

Two orthogonally mounted airfoil shear sensors on the RSVP measured the velocity shear microstructure (u_z and v_z). The spatial resolution of these probes, approximately 0.03 m [*Osborn and Crawford*, 1980], can resolve most of the Kolmogorov shear spectrum [*Tennekes and Lumley*, 1992] for typical oceanic turbulence levels. The velocity shear spectra were integrated for wave numbers between 2.5 and 40 cycles per meter (cpm) to estimate the turbulent kinetic energy dissipation rate (ε) at approximately 1.7-m depth intervals (2 s of data). This dissipation rate is related to the microscale shear variance by

$$\varepsilon = 7.5\nu \left(\frac{\langle u_z^2 \rangle + \langle v_z^2 \rangle}{2} \right) \quad (1)$$

where ν is the kinematic viscosity of seawater, approximately 1.85×10^{-6} m^2 s^{-1} for these temperatures and salinities, and the angle brackets $\langle\ \rangle$ indicate vertical averaging. The factor 7.5 results from assuming that the velocity fluctuations are isotropic [*Tennekes and Lumley*, 1992]. This assumption is generally valid when ε is sufficiently large that the buoyancy or "Ozmidov" length scale $L_b = (\varepsilon/N^3)^{1/2}$, is much greater that the viscous or "Kolmogorov" scale, $L_k = (\nu^3/\varepsilon)^{1/4}$ [*Dillon*, 1984]. This condition can be written in terms of an "activity" index $A_T = \varepsilon/\nu N^2$: if A_T is greater than about 24 [*Stillinger et al.*, 1983], then a significant fraction of the total velocity shear variance will be found at spatial scales that are unaffected by buoyancy.

Prior to calculating ε, the velocity shear records were edited for obvious spikes resulting from anomalous fall speeds or encounters with biota. Additionally, shear values greater than 3 standard deviations from the mean shear for each 2-s interval were excluded from the variance calculations, since the majority of these large shears were believed to be related to biota impacts or electronic noise. For ε above the noise floor of about 2×10^{-9} m^2 s^{-3}, this latter stage of editing made little difference to the estimates of ε.

To provide background information on thermal structure and internal gravity waves, an ice-mounted mooring consisting of 15 miniature data recorders (MDRs) was deployed twice, with the positions of some sensors being changed between deployments. The mean depths of the MDRs over 2-day intervals are shown in Figure 2b for both deployments. A Yellow Springs Instruments model YSI40006 thermistor was installed in each MDR. The MDRs have a resolution of approximately 0.001°C and a long-term stability of 0.03°C. In the deepest MDR, a Veritron Corp. model 3000 pressure sensor was installed to monitor the mooring motion. This pressure sensor had a resolution of 0.5 psi (~0.3 m). The variations in the sensor depths near $t = 87$ and 145 in Figure 2b are due to mooring motion. The depths of sensors above the bottom MDR were interpolated using a mooring model forced by a depth-independent, ice-relative current. Temperature was recorded at 2-min intervals by the upper 14 MDRs, and both T and P at 4-min intervals by the deepest MDR. Sensors were calibrated before and after the experiment.

Additional data collected at ISW by other investigators included ISW location, water depth, currents, CTD profiles, and meteorological and ice data [*Gordon et al.*, 1993b]. The drift track of the camp (Figure 1) is based

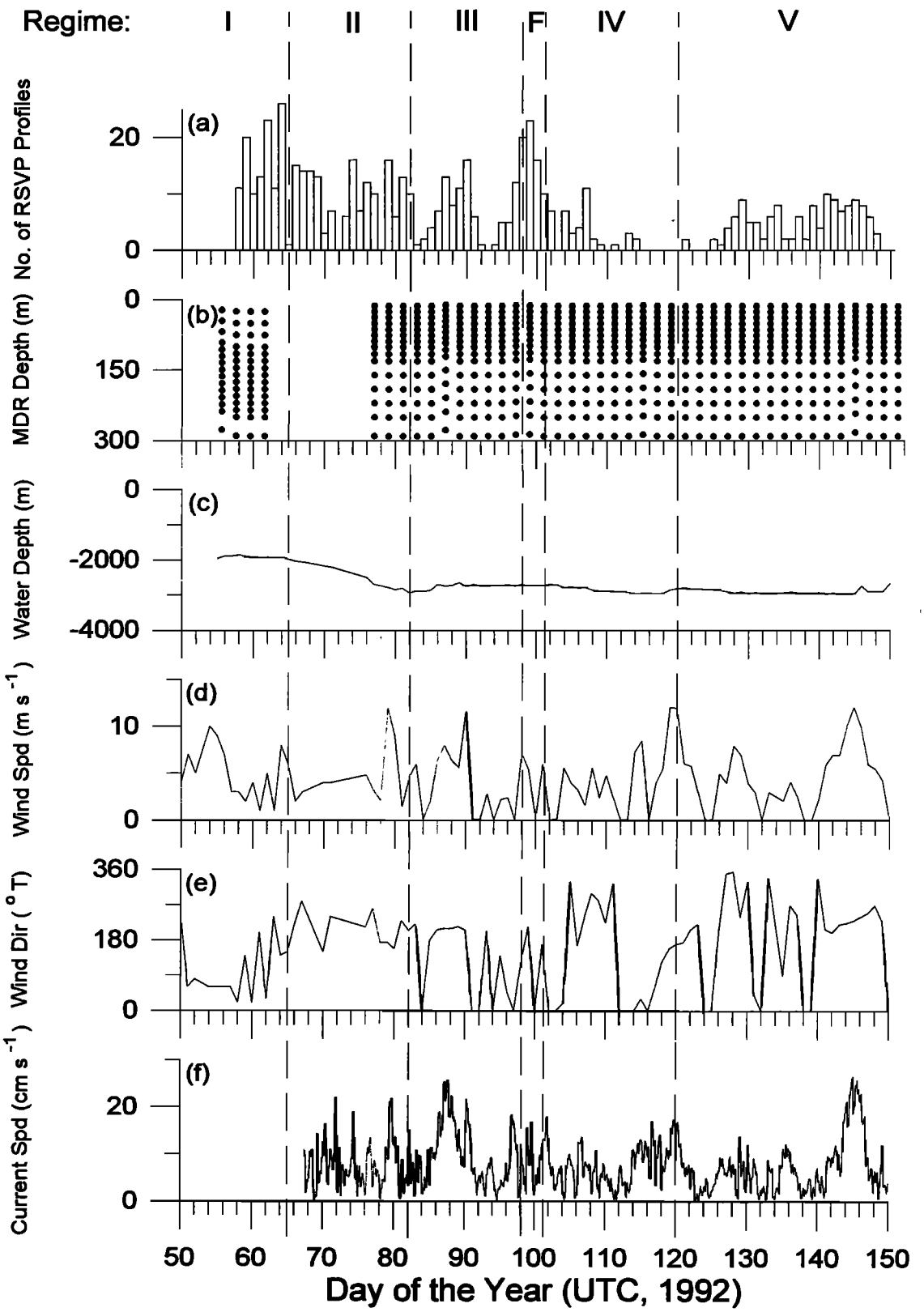

Figure 2. (a) Number of RSVP profiles per day, (b) MDR depths, every two days, (c) water depth (m), (d) wind speed (m s^{-1}), (e) wind direction (°T), and (f) ice-relative current speed at 50 m (cm s^{-1}) at ISW.

on global positioning system (GPS) measurements after smoothing with the complex demodulation algorithm described by *McPhee* [1988]. A precision depth recorder and an acoustic pinger mounted on the LDEO CTD wire were used to determine water depths. To supplement water depth measurements at ISW, satellite and aircraft gravimetric data were used by *LaBreque and Ghidella* [1993] to develop a bathymetric chart for the western Weddell Sea. Current velocities at ISW were measured at three depths under the ice, 25, 50 (Figure 2f), and 200 m [*Muench et al.*, 1993]. CTD profiles to the bottom were collected by LDEO roughly at 10 km intervals along the drift track, i.e., several times per week [*Gordon et al.*, 1993b; *Huber et al.*, 1994].

3. ISW Upper Ocean Hydrography

The hydrographic structure of the upper ocean helps determine the physical processes that can cause the vertical transport of heat and salt. We therefore first review the principal features of the upper ocean hydrography at ISW. For reference, a profile taken at $t = 76.018$ is shown (Figure 3). A thin, well-mixed surface layer that was present during the earlier portion of the experiment typically extended to a depth of 20–50 m and was bounded below by the seasonal pycnocline. Below the seasonal pycnocline, a weakly stratified layer was found. This layer had potential temperatures (-1.9° to -1.5°C) and salinities (typically 34.3 to 34.6 psu) that are characteristic of the Winter Water layer described by *Foster and Carmack* [1976b] and *Muench et al.* [1990]. This layer is believed to be a remnant of the surface mixed layer from the previous winter. The lower portion of this layer has been, and continues to be, modified substantially by intrusions and vertical mixing. Intrusions like those in Figure 3a were typically found between 150 and 300 m depth throughout the experiment. They are clearly visible in θ-S diagrams (e.g., Figure 3b) as kinks in the θ-S curve. Below this weakly stratified layer was the permanent pycnocline, which was roughly 300 m thick with a potential density change of about 0.08 kg m^{-3}. The maximum buoyancy frequency N in the permanent pycnocline was about 2 cycle per hour (cph). Within both the permanent pycnocline and the region of intrusions, double-diffusive steps were found.

Below the permanent pycnocline there was a core of relatively warm water with a potential temperature ranging from 0.4° to 0.6°C and a salinity of 34.68–34.70 psu. This water lies within the θ-S space denoted as Warm Deep Water (WDW) by *Foster and Carmack* [1976b]. The maximum potential temperature (θ_{max}) and salinity (S_{max}) values and their depths ($Z_{\theta max}$ and Z_{Smax}) (Figure 4) were determined from the CTD profiles collected by LDEO and kindly provided by A. Gordon. The value of θ_{max} generally decreased as the ice camp moved north [*Gordon et al.*, 1993a]. During the first few days of the camp, both θ_{max} (~0.5°C) and S_{max} (34.67–34.68) were lower than elsewhere along the drift path. Also during this period, both the permanent pycnocline and the $Z_{\theta max}$ were approximately 200 m deeper than during the remainder of the experiment. The Z_{Smax} was observed to be about 200 m deeper than $Z_{\theta max}$ during most of the experiment, a feature also found in the eastern Weddell Sea [*Gordon and Huber*, 1990].

Analysis of CTD data from the main camp and cross-slope helicopter transects indicates that ISW generally drifted near the warm core of the northward-flowing western arm of the Weddell Gyre [*Gordon et al.*, 1993a; *Muench and Gordon*, 1995]. Measurements from early in the experiment were inshore of the warm core of the current, which roughly follows the 2500-m isobath. On the basis of changes in bathymetry and upper ocean hydrographic structure, the experiment was divided into five time periods or regimes (see Figures 1, 2, and 4 and Plate 1).

Regime I ($57 \leq t < 65$): The ice camp traveled over the upper continental slope, where water depths were less than 2000 m. There was a thin, deep seasonal pycnocline (~50–75 m) and $Z_{\theta max}$ was near 800 m.

Regime II ($65 \leq t < 82$): The ice camp drifted across the continental slope into deeper water with the water depth increasing from 2000 to 2700 m. There was a shallower seasonal pycnocline (~30 m) and $Z_{\theta max}$ (~700 m) than in regime I.

Regime III ($82 \leq t < 101$): The seasonal pycnocline was weaker than in the previous regimes with a typical density difference across the seasonal pycnocline of 0.05–0.1 kg m^{-3}, compared with differences of approximately 0.2 earlier in the experiment. This decrease in density difference was caused by an increase in salinity and a slight decrease in temperature in the surface layer. This temperature decrease (~0.03°C) is apparent in the MDR records but is not noticeable in Plate 1a. The temperature maximum was shallower than in regimes I and II ($Z_{\theta max} \sim$ 600–650 m). The ice station traveled over a deeper portion of the continental slope during this period.

Regime IV ($101 \leq t < 120$): During this regime, the upper water column was in transition from regime III to V with a very weak seasonal pycnocline. The $Z_{\theta max}$ was at ~ 650–700 m, a slight deepening relative to regime III. This regime is also characterized by extremely variable ice drift (Figure 1) compared with the relatively smooth northward motion during regimes III and V. Analyses of measured and geostrophic currents [*Muench and Gordon*, this issue] indicated a strong inflow of about 9 Sv from the east during this period, possibly associated with bathymetric steering of the primarily barotropic currents by Endeavor Ridge.

Regime V ($120 \leq t < 150$): The seasonal pycnocline was absent, and ISW remained over a deeper portion of the continental slope. The upper mixed layer now included the remnant mixed layer from the previous winter. The water column below 200 m was similar to that in regime IV.

The LDEO profiles from regimes IV and V have been averaged together to produce representative profiles (Figure 5a). The lack of a seasonal pycnocline during these regimes is apparent, especially when compared with Figure 3a, which is a profile taken from regime II.

In a 12 hour period on Day 99, near the end of regime

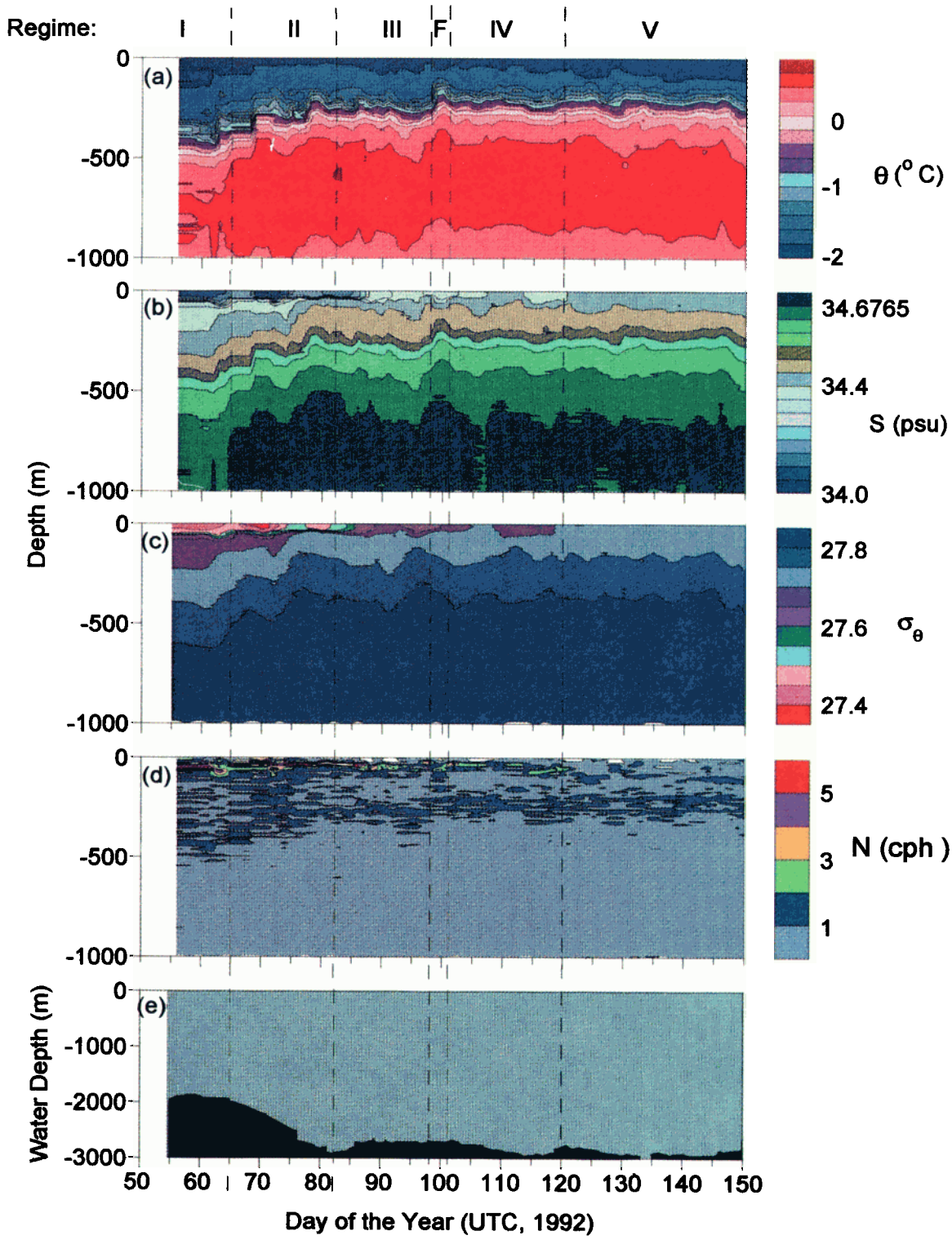

Plate 1. Transects along the ISW drift track of (a) potential temperature θ (°C), (b) salinity S (psu), (c) potential density σ_θ, (d) buoyancy frequency N (cph), and (e) water depth D (m) from the LDEO profiles.

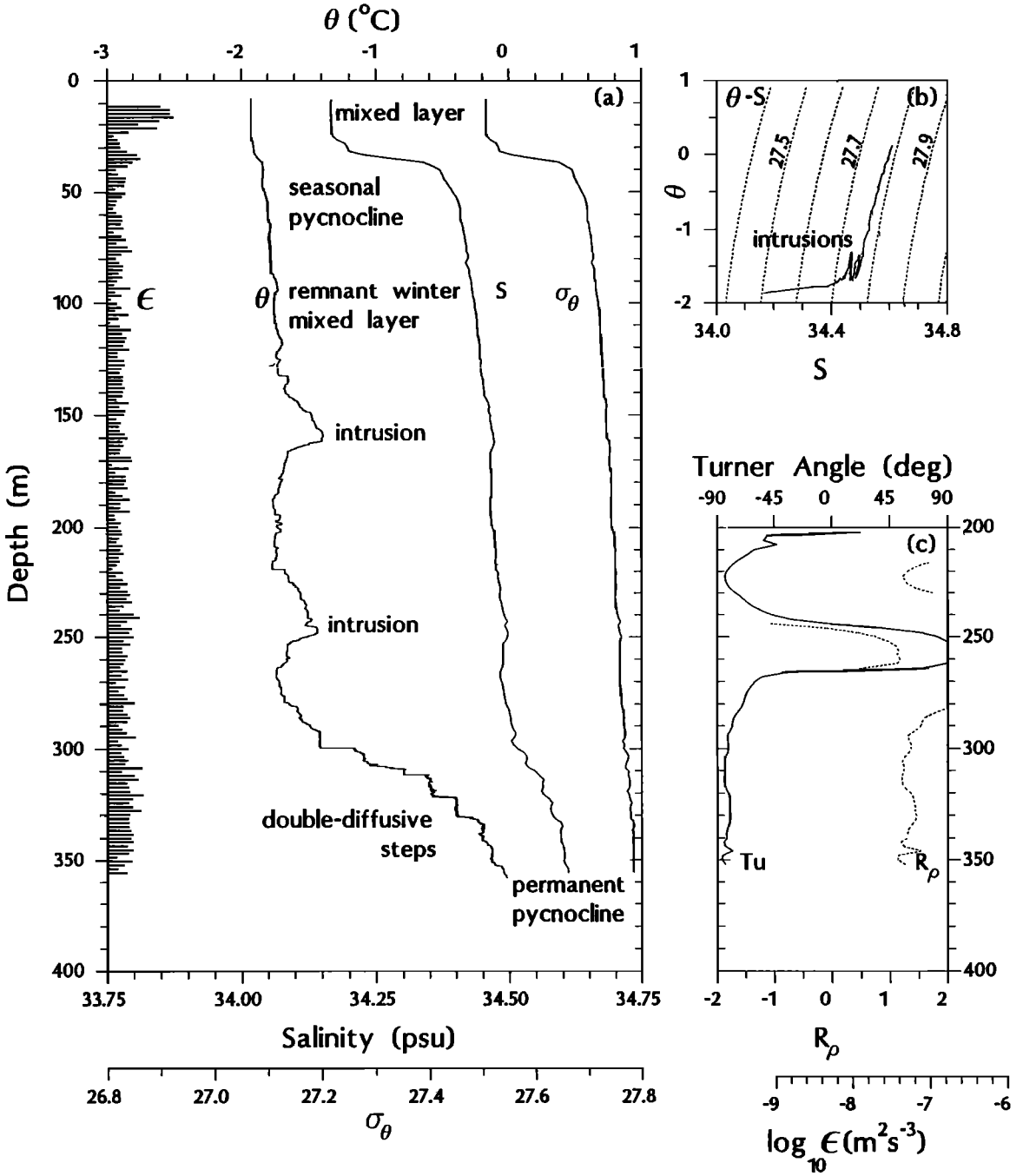

Figure 3. (a) Profiles of potential temperature θ (°C), salinity S (psu), potential density σ_θ, and the log of the dissipation rate ε (m^2 s^{-3}) collected on $t = 76.0184$; (b) the θ-S diagram for this profile, with constant density lines shown dotted; and (c) density ratio R_ρ and Turner angle Tu (°).

III, ISW passed over an unusual hydrographic feature (denoted in Figures 2 and 4 and Plate 1 by "F"). This feature, which might be a small eddy, has been excluded from further analyses of these data.

4. Vertical Mixing Processes and Rates

The primary purpose of this study was to investigate the rate of heat transport from the subsurface Warm Deep Water (WDW) to the ocean surface. We concentrated on processes which occur within the permanent and seasonal pycnoclines, since they act as barriers for heat flux. In this section we first discuss the heat transport processes expected to be important in the permanent pycnocline, then review the transport mechanisms in, and the destruction of, the seasonal pycnocline.

4.1. The Permanent Pycnocline

On the basis of the hydrographic structure discussed in the previous section, the most likely processes respon-

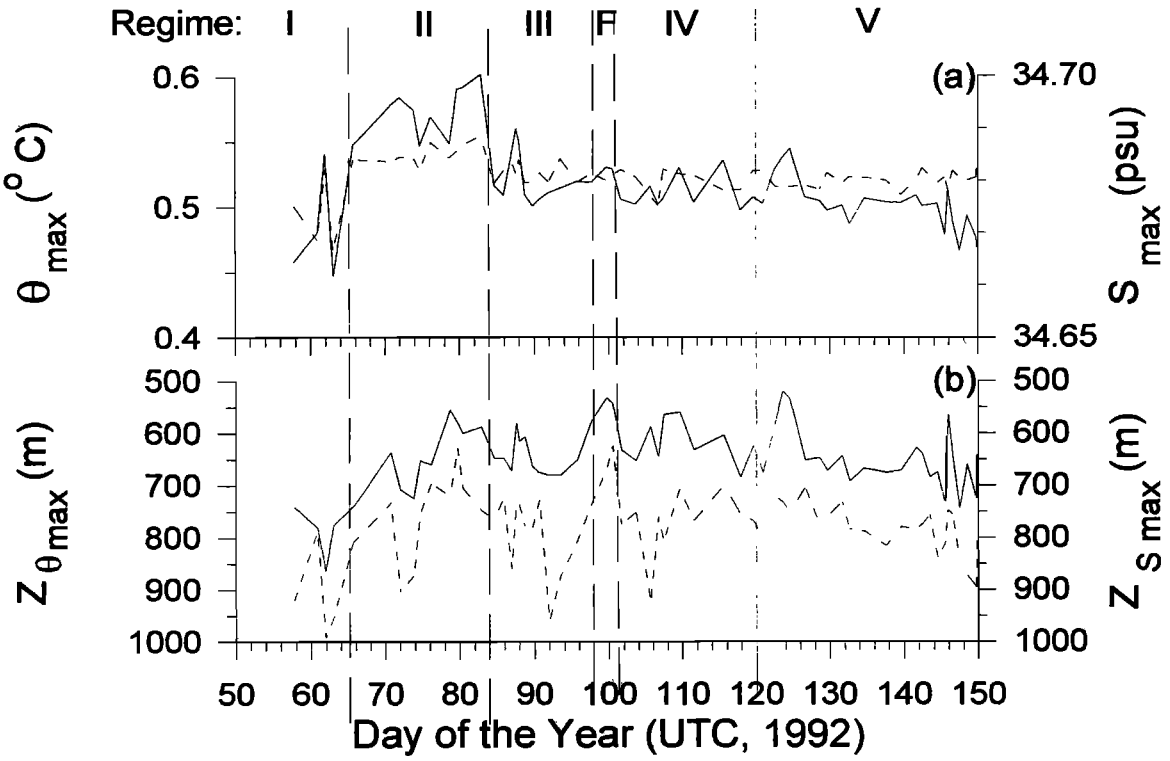

Figure 4. (a) The maximum potential temperature θ_{max} (°C) (solid line) and salinity S_{max} (psu) (dashed line) as observed at the camp from LDEO CTD profiles. (b) Also shown are depth of θ_{max}, $Z_{\theta max}$ (solid line) and depth of S_{max}, Z_{Smax} (dashed line).

sible for heat transport through the permanent pycnocline are double-diffusion, internal wave-induced shear instabilities, and intrusions. These are discussed independently below.

Double Diffusion. Double-diffusive staircases are often found when the vertical gradients of T and S have the same sign [see *Turner,* 1973; *Schmitt,* 1994]. If T and S both decrease with depth, salt fingering may occur; if T and S both increase with depth, double-diffusive convection is possible. We will concentrate on the latter case since in polar regions, cold, fresh water generally lies above warmer, saltier water. Salt fingering is possible, however, below the temperature and salinity maxima and also on the lower edges of warm, salty intrusions.

In double-diffusive convection (see Figure 3), the density gradient due solely to the temperature stratification is intrinsically unstable, while the salinity gradient provides the necessary static stability. Staircases are characterized by homogeneous layers that are bounded above and below by thin interfaces (or "sheets") in which both T and S change rapidly with depth. The layers are convectively stirred by the destabilizing buoyancy flux arising from the diffusive transport of heat through the interfaces, which is only partly offset by the diapycnal salt flux. This combination of diffusion and convection can significantly increase the diapycnal fluxes of heat, salt, and momentum.

One indicator of double-diffusive activity is the Turner angle (Tu), defined by

$$Tu = \tan^{-1}\left(\frac{(1+R_\rho)}{(1-R_\rho)}\right) \tag{2}$$

where R_ρ is the density ratio, given by

$$R_\rho = \frac{\beta\ \partial S/\partial z}{\alpha\ \partial T/\partial z} \tag{3}$$

In (3), β and α are the haline contraction and thermal expansion coefficients, respectively. A Turner angle between -90° and -45° indicates a potential for double-diffusive convection; a value between +45° and +90° indicates potential for salt fingering. As Tu approaches -90°, which implies that the destabilizing density gradient due to $\partial T/\partial z$ is becoming comparable to the stabilizing gradient due to $\partial S/\partial z$, the likelihood of finding strong double-diffusive activity increases [*Ruddick,* 1983]. Equivalently, values of R_ρ greater than 1.0 are indicators of double-diffusive activity, with $1.0 < R_\rho < 2.0$ indicating strongly double-diffusive conditions. For salt fingering, $0.0 < R_\rho < 1.0$. Favorable conditions for double-diffusive convection were found in a band below about 200–250 m during regimes I and II and below about 100–150 m during regimes III to V (Figures 6a, 3c, 5b, and 5c). Double-diffusive steps were frequently found in this band, some examples of which can be seen in Figure 3a.

Observed step heights varied from ~0.05 m, near the vertical resolution of the RSVP's temperature sensor, to about 20 m, although most steps had heights less

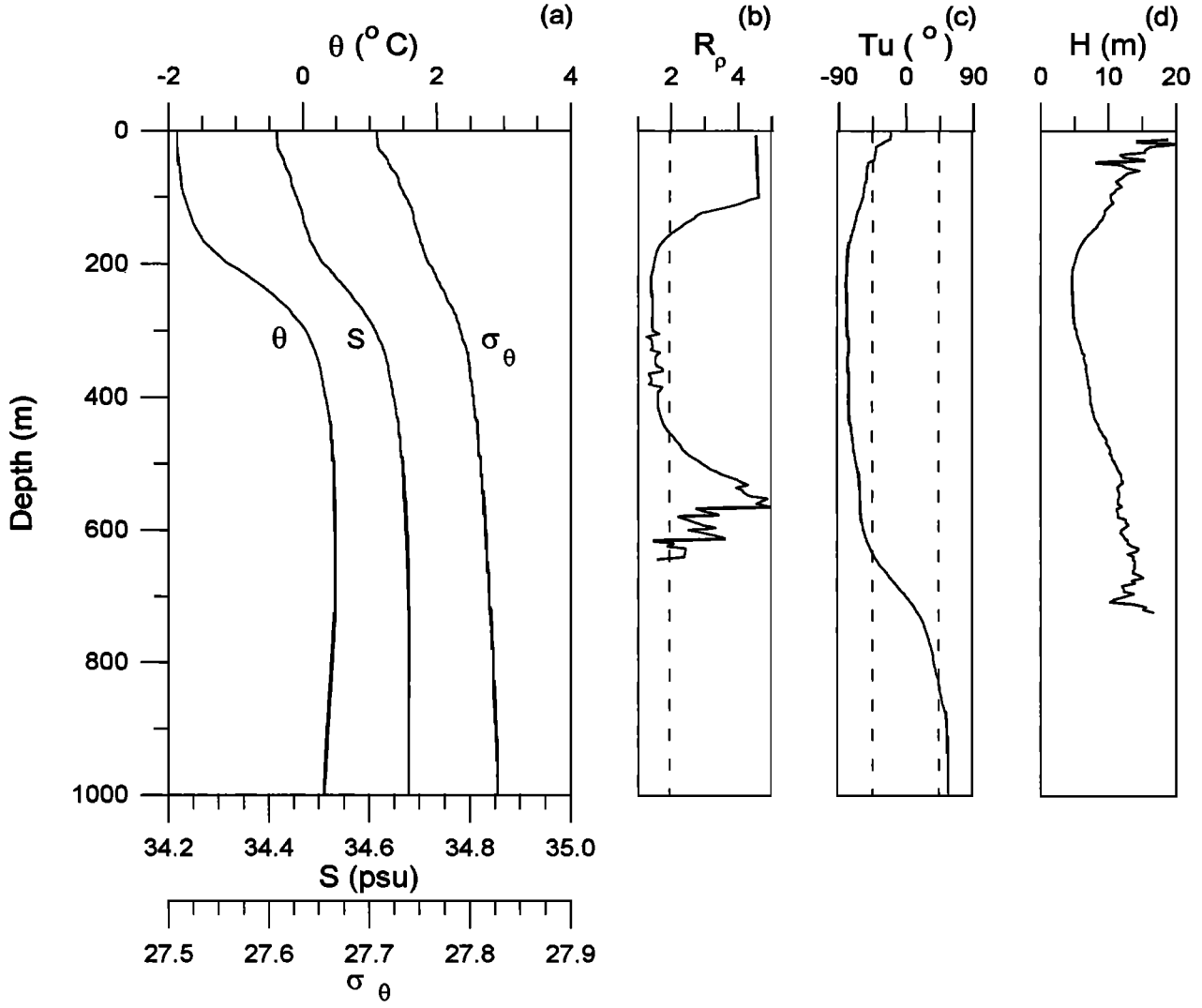

Figure 5. Average profiles for regimes IV and V for (a) potential temperature θ (°C), salinity S (psu), and potential density σ_θ ; (b) density ratio R_ρ; (c) Turner angle Tu (°); and (d) modeled step height H (m). Thirty-three LDEO profiles were used for the averages.

than 10 m. The temperature differences across interfaces adjacent to thick layers (5–10 m) typically ranged from 0.1° to 0.5°C and occasionally reached 0.8°C. The largest temperature steps were usually associated with large intrusions. Intrusions and double-diffusion interact: intrusions establish the large-scale conditions necessary for the double-diffusive instability, and double diffusion supplies a driving force for intrusions [*Toole and Georgi,* 1981; *Walsh and Ruddick,* 1995].

Smaller steps, with heights of about 2 m and temperature differences less than 0.1°C, were observed in regimes II to V and were much more common than the larger steps. Double-diffusive steps have been previously observed in the Weddell Sea by *Foster and Carmack* [1976a] and *Muench et al.* [1990]. The latter paper divided steps into two size classifications: type A (1–5 m) and type B (> 10 m). The most common size steps observed here correspond to type A. *Muench et al.* [1990] found that type B steps typically occurred deeper than type A in the weaker stratification just above the broad temperature maximum. If such steps were present in the western Weddell, they would have been present below the maximum depth sampled by the RSVP. The larger steps observed here are more likely to be related to intrusions than to type B steps, which were found only in a more central region of the Weddell Gyre where no intrusive features were present.

Models for estimating the vertical heat flux (F_H) through double-diffusive steps have been developed by several investigators, including *Marmorino and Caldwell* [1976], *Taylor* [1988], *Fernando* [1989], *Kelley* [1990], and *Rudels* [1991]. We refer to these studies as MC76, T88, F89, K90, and R91, respectively. The heat fluxes predicted by each model are denoted F_{H-MC}, F_{H-T}, F_{H-F}, F_{H-K}, and F_{H-R}, respectively. All of these formulations are parameterized using the temperature difference across the step ($\Delta\theta$) and the density ratio R_ρ (3). (These investigators use ΔT in their heat flux formulations; however, the formulas are quoted with $\Delta\theta$ here.) With the exception of F89, the models

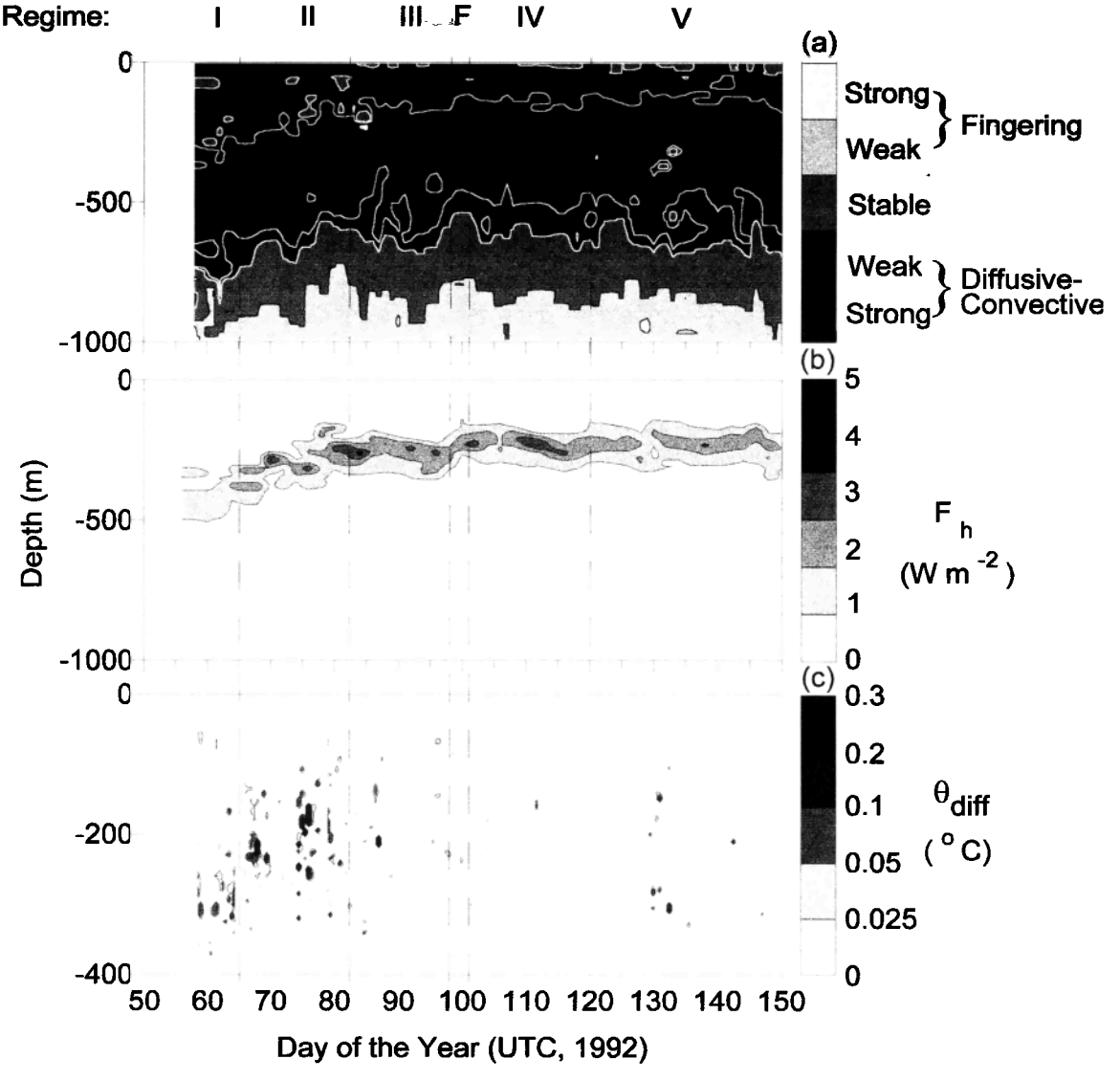

Figure 6. Transects of (a) the Turner angle Tu; (b) vertical heat flux F_H (W m^{-2}) according to the formulation of Kelley [1990]; and (c) locations of major intrusions (see text). In (c) the lower line is the $\sigma_\theta = 27.78$ isopycnal and the upper line is the $\sigma_\theta = 27.70$ isopycnal. Tu is scaled with strong salt fingering as $67.5 < Tu < 90$, weak salt fingering as $45 < Tu < 67.5$, stable as $-45 < Tu < 45$, weak diffusive-convective as $-45 < Tu < -67.5$ and strong diffusive-convective as $-67.5 < Tu < -90$.

assume that the heat flux is proportional to $(\Delta\theta)^{4/3}$, based on a model developed for heat flow between two parallel plates [*Turner*, 1973]. Heat flux parameterizations (in W m^{-2}) for four of these models are presented below:

$$F_{H-MC} = 0.00859\,\rho_0\,c_p\,\alpha^{-1} \cdot \exp\{4.6\exp[-0.54(R_\rho - 1)]\} \cdot (g\kappa_t^2\nu^{-1})^{1/3}\,(\alpha\Delta\theta)^{4/3} \quad (4)$$

$$F_{H-T} = 0.00272\,\rho_0\,c_p\,\alpha^{-1}\,R_\rho^{-2.1} \cdot (g\kappa_t^2\nu^{-1})^{1/3}\,(\alpha\Delta\theta)^{4/3} \quad (5)$$

$$F_{H-K} = 0.0032\,\rho_0\,c_p\,\alpha^{-1}\exp[4.8R_\rho^{-0.72}] \cdot (g\kappa_t^2\nu^{-1})^{1/3}\,(\alpha\Delta\theta)^{4/3} \quad (6)$$

$$F_{H-R} = \frac{5}{3}\pi^{-5/3}\,\rho_0\,c_p\,\alpha^{-1}[1-(\kappa_s\kappa_t^{-1})^{0.5}]^{4/3} \cdot (g\kappa_t^2\nu^{-1})^{1/3}\,(\alpha\Delta\theta)^{4/3} \quad (7)$$

where ρ_0 is the mean density (kg m^{-3}), c_p is the specific heat (J kg^{-1} °C^{-1}), g is the gravitational acceleration (m s^{-2}), and κ_s and κ_t are molecular diffusivities (m^2 s^{-1}) for salt and heat, respectively. The parameterization by F89 is only self-consistent for a specific value of R_ρ (≈ 1.2) and therefore has not been

used. (However, readers interested in the physical processes involved in double-diffusive convection with varying density ratio will find a clear description in that paper.) The model of R91 was developed for $R_\rho = 1.0$; consequently, it should only be applied to regions of low R_ρ.

For regions of fairly constant R_ρ, the fundamental parameter required for estimating the double-diffusive heat flux is the thermal step at the interface, $\Delta\theta$. Methods for locating interfaces have been developed for application to data from the Arctic Ocean [*Padman and Dillon,* 1987, 1988]. Automated searching in the present data is, however, complicated by the wide range of step scales, the intermittency of steps, and the irregular structure in the interfaces separating the quasi-homogeneous layers. The thermal step $\Delta\theta$ was estimated from the layer height H using $\Delta\theta = \langle\partial\theta/\partial z\rangle H$. Two methods were followed to determine the thermal gradient and H.

1. For the range of temperatures for which steps were commonly found, each profile was categorized as consisting of "large," "medium," and "small" steps, based on visual inspection of profiles and ignoring layers less than 0.5 m thick. The layer thickness, H, for each category was then estimated from a more detailed inspection of several typical profiles for each category. The mean thermal gradient was estimated using the difference in θ over the depth range in which steps were found.

2. We estimated H from the large-scale stratification parameters using the relation proposed by *Kelley* [1984]:

$$H = \left[0.25 \times 10^{-9}\, R_\rho^{1.1}\, \nu\, \kappa_T^{-1}\, (R_\rho - 1)\right]^{0.25} \cdot \left(\kappa_T \langle N^{-1}\rangle\right)^{0.5} \quad (8)$$

The thermal gradient was then estimated from a vertically smoothed average of θ, where the averaging scale was much greater than a typical layer height.

For regimes II to V, mean layer heights evaluated using method 1 are about 2 m, and for the mean thermal stratification of 0.015°C m^{-1}, the resultant value of $\Delta\theta$ is 0.03°C. Examples of step heights obtained using method 2 are shown in Figure 5d, and in the region of well-defined steps (Tu near -90°) step heights range from 4–7 m. In sections of the profiles with well-defined steps, the step heights from both methods were similar. However, when the steps are poorly defined or absent, the heights from method 1 are much lower than the modeled heights from method 2.

To demonstrate the differences between the heat flux models described by (4)–(7), and to define a reasonable upper bound on double-diffusive fluxes, we apply each model to the layer heights determined by method 2 (Figure 7). Both K90 and T88 predict essentially the same values, hence the T88 estimates are not shown. Heat flux estimates from R91 are only shown in Figure 7 when $R_\rho < 1.5$. The estimates made using MC76 exceed those using K90 (Figure 7) by a factor of 2–2.5 for $1.4 < R_\rho < 1.5$ (typical values for these data). At $R_\rho = 1.0$, the MC76 and K90 predictions differ by a factor of 4. For $1.0 < R_\rho < 1.5$ there is a wide scatter in the laboratory data on which these formulations are based, with very little data available at all for $R_\rho < 1.2$. The discrepancy between these models is therefore explained primarily by the authors' different choices of functions for fitting the R_ρ dependence. Note, however, that MC76 heat flux exceeds those from R91 (Figure 7), the latter being assumed to be an upper bound because it is formally applicable only at neutral static stability; i.e., $R_\rho = 1$.

The heat fluxes evaluated using method 1 for the mean layer height range from 1 to 2 W m^{-2}. Note that this is an average over the depth range for which steps are found. This is comparable to the heat flux estimate using method 2 (Figure 7) when averaged over the diffusive-convective depth range. Our interpretation, based on our observations of both layer heights and intermittency, is that the double-diffusive flux is 1–2 W m^{-2} on average, with peak values, when steps are well-defined, of about 4 W m^{-2}.

Ideally, the flux laws above should be applied to the properties ($\Delta\theta$ and R_ρ) of each observed diffusive-convective step, followed by averaging of the modeled fluxes appropriate time and/or depth ranges (see, for example, *Padman and Dillon* [1987]). In the present case, however, the steps are difficult to find automatically in the RSVP data due to their intermittency and the variability of their sizes, as discussed above. Furthermore, steps are seldom resolved by the LDEO CTD data, which have been used here to extend our flux calculations to the depth of the temperature maximum. *Padman and Dillon* [1987] found for Arctic data that the actual mean heat flux was about 50% higher than would be predicted from (4) and (8), primarily because the large steps in the measured distribution of temperature differences dominated the average flux due to the $\Delta\theta^{4/3}$ dependence in (4)–(7). Analyses on a few characteristic profiles in the present data set suggest that some increase in mean heat flux would occur by considering the true distribution of interfacial $\Delta\theta$ and R_ρ; however, the increase is small, less than 20%.

Transects of F_{H-K} obtained using method 2 are shown in Figure 6b. Maximum fluxes were reasonably constant throughout all regimes, although the heat flux of regime I was slightly smaller. Maximum fluxes of 4 W m^{-2} (following K90) occurred in a band centered near 250 m in regimes III–V. In regime II, this band was approximately 50 m deeper (300 m), which corresponds to the deeper location of the band of double-diffusive steps. Likewise, the band was significantly deeper (~400–450 m) in regime I and the heat fluxes were smaller (< 3 W m^{-2}). The maximum heat flux of 4 W m^{-2} corresponds to a buoyancy flux of about 4×10^{-10} m^2 s^{-3}. T88 noted that the buoyancy flux should be approximately balanced by the dissipation rate ε in the layers, however we are unable to test this hypothesis in the present case because the expected buoyancy flux is less than the noise level for ε.

In data obtained from the Canada Basin, *Padman and Dillon* [1988] were able to trace individual layers

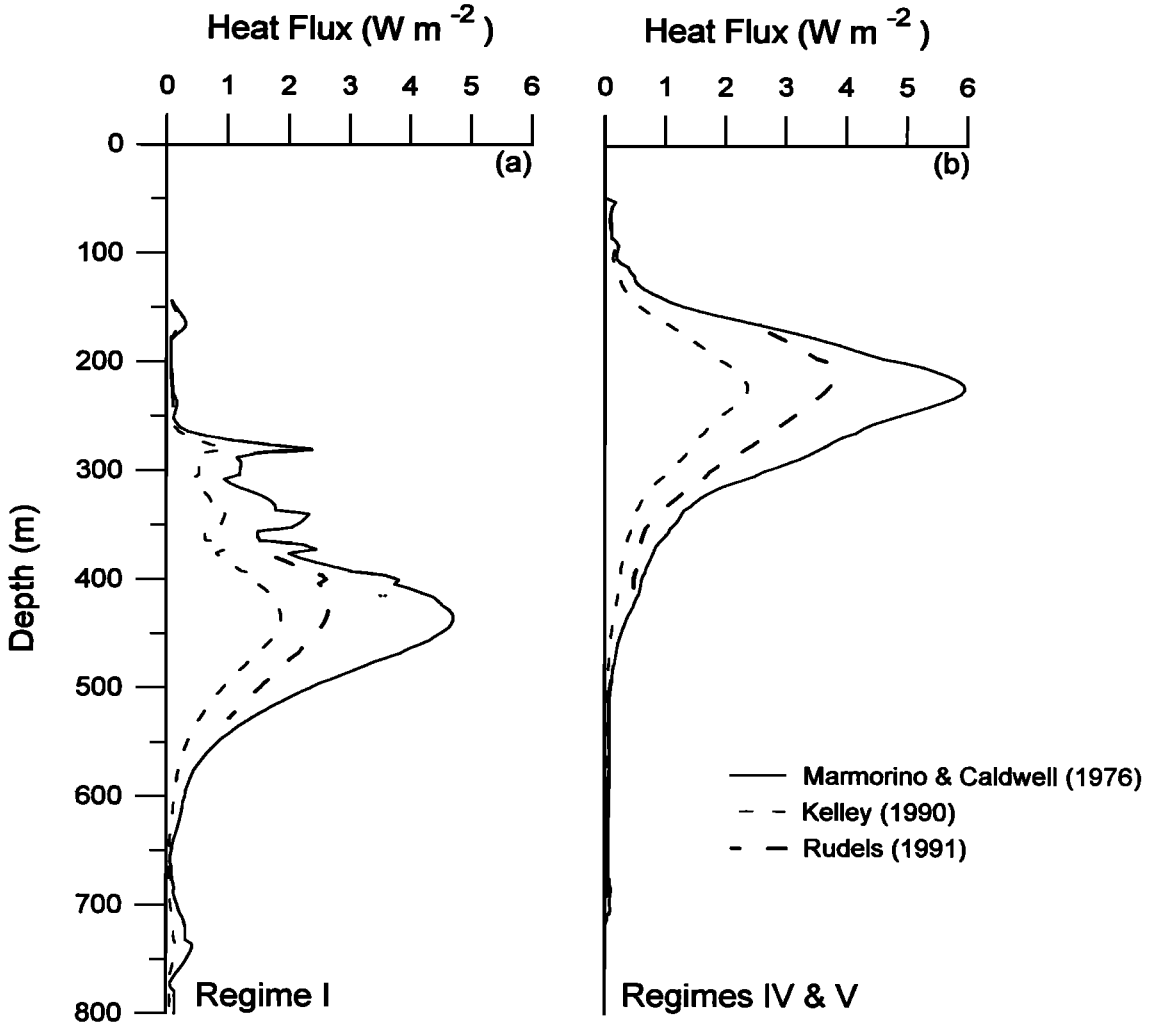

Figure 7. Intercomparison of heat flux estimates from the formulations of *Marmorino and Caldwell* [1976] (solid line), *Kelley* [1990] (dashed line), and *Rudels* [1991] (heavy dashed line) for representative profiles from (a) regime I and (b) regimes IV and V. (Note that heat flux estimates from Rudels are only shown for $R_\rho < 1.5$.)

between adjacent profiles, allowing estimates of along-layer variability of T and H to be made. With the present data set, however, this is not possible. This may be due to the relatively rapid motion of the ice camp, combined with significant horizontal spatial gradients of T and S in the steps. Temporal evolution may also be more rapid because vertical heat fluxes are much higher here, being $O(1)$ W m^{-2} compared with 0.04 W m^{-2} in the Canada Basin. *Muench et al.* [1990] noted that the large (type "B") steps found to the east of the ISW drift track were observable over hundreds of kilometers in CTD data, however individual layers were not traced.

Below the salinity maximum (Plate 1b), gradients of both T and S are favorable for salt fingering. The Turner angle, however, indicates only weak salt fingering conditions (Figure 6a).

Shear Instabilities. In the permanent, midlatitude thermocline, a significant component of the total diapycnal flux is usually provided by mixing associated with shear instabilities of the internal gravity wave field [*Gregg,* 1989]. In the few experiments from polar regions that have investigated both mixing and internal waves, a wide range of diapycnal heat fluxes have been found. For example, *Padman and Dillon* [1987] found that the contribution of shear-driven mixing to the local diapycnal flux was negligible (less than 0.1 W m^{-2}) in the central Canada Basin. In contrast, measurements in the eastern Arctic revealed heat fluxes of up to 30 W m^{-2} due to energetic mixing events associated with large-amplitude, high-frequency wave packets [*Padman and Dillon,* 1991]. One difference between these two sites is their proximity to internal wave sources. The measurements described by *Padman and Dillon* [1991] were made in a region where strong tidal flows were able to interact with the steep topography of the continental slope, whereas the Canada Basin measurements were taken well away from significant topographic features.

Given our poor understanding of both the topography and currents in the western Weddell Sea prior to

the present program, it was not known whether current/topography interactions would be important in this region. In the observed microstructure profiles the dissipation rate ϵ in the permanent pycnocline never exceeded the noise level of about 2×10^{-9} m^2 s^{-3}. What would be the heat flux if the true value of ϵ was always near the noise level? Following *Osborn* [1980], we estimate the effective diapycnal eddy diffusivity as

$$K_t \approx \frac{\Gamma \epsilon}{N^2} \tag{9}$$

where Γ is the mixing efficiency, generally assumed to be about 0.2 [*Gregg*, 1987]. For a buoyancy frequency $N = 1$ cph (0.0017 s^{-1}), the diffusivity associated with the noise level for ϵ is about 10^{-4} m^2 s^{-1}. Since the diapycnal heat flux is given by

$$F_H = \rho\, c_p\, K_t \frac{\partial T}{\partial z} \tag{10}$$

the noise level of ϵ is equivalent to a heat flux of about 4 W m^{-2}. This value is, however, an upper bound. Shear-driven turbulence tends to be extremely variable in both space and time [*Baker and Gibson*, 1987], with the average value being dominated by the presence of a few large but intermittent events. Since we do not find any events significantly above the noise floor, we expect that the mean value of heat flux is actually much less than 4 W m^{-2}. An alternative technique for estimating the vertical diffusivity and heat flux from internal wave parameters based on a model by *Gregg* [1989] and extended by *Wijesekera et al.* [1993], implies a mean heat flux of about 1 W m^{-2}.

Intrusions. Intrusions, such as those shown in Figure 3, are often associated with large along-isopycnal gradients of temperature and salinity, and hence are frequently found at fronts between contrasting water types. Isopycnal mixing can be quite energetic and effective, since it does not have to overcome any buoyancy gradient. It is, however, extremely difficult to evaluate its magnitude: *Ledwell et al.* [1993] is one of very few studies to have estimated an isopyncal diffusivity by tracking the lateral diffusion of released tracers. In the present study we are unable to quantify the mixing rates suggested by the presence of intrusions. However, intrusions can play an important role in the ultimate ventilation of the subsurface oceanic heat to the sea surface.

During ISW, large intrusions were frequently found in the weakly stratified region above the permanent pycnocline. An intrusion is most accurately identified as a region of anomalous θ-S characteristics relative to some "background" θ-S relation. The background relationship can be determined by scale separation (see, for example, *Ruddick and Walsh* [1995]), or by averaging several profiles together to define a "mean" state. In the present study, the mean hydrography varies in the vertical on scales comparable to intrusion heights, hence the former method is impractical. The latter method is also difficult to apply in this case because of the rapid change in "mean" hydrographic properties in the region where most intrusions are found. Since our present goal is simply to describe the distribution of intrusions, we search for regions where the temperature decreases with increasing depth, contrary to the large-scale trend of increasing θ (above the temperature maximum). For such regions, we calculate the maximum value of $\Delta\theta$ representing the difference between a local temperature maximum and the adjacent (in depth) local minimum. These values are contoured from the RSVP data in Figure 6c. Note that, according to our search algorithm, locally high values of $\Delta\theta$ occur on the lower edges of warm and salty intrusions. Most intrusions are found in regimes I and II, i.e., while ISW was located over the upper slope. This observation is consistent with most intrusions being located on the inshore side of the warm-core current, between this current and the shelf/slope front revealed by the cross-slope transect in the work by *Muench and Gordon* [this issue].

We also indicate on Figure 6c two isopycnals that represent the approximate upper and lower bounds of intrusive activity. The lower isopycnal, $\sigma_\theta = 27.78$, slopes upward both to the west (inshore) and east of the warm core, reaching the bottom of the winter mixed layer over the upper slope and in the central Gyre. Isopycnal mixing associated with the intrusions therefore provides a mechanism for venting upper WDW heat to the surface over a broader region than would be possible by diapycnal (near-vertical) fluxes alone. A similar mechanism has been described by *Boyd and D'Asaro* [1994] for explaining the heat lost by the West Spitsbergen Current as it enters the Arctic Ocean.

Large intrusions, defined by us as having heights of 25–35 m and temperature anomalies of 0.1°–0.6°C (see Figure 8) were usually found in regimes I and II. Smaller intrusions with heights of 5–20 m and smaller temperature anomalies were found in all regimes but may not appear in Figure 6c because of the analysis method.

In general, intrusions could not be tracked between RSVP profiles to allow estimations of their horizontal extent or lifetime. However, the horizontal extent of the intrusions in a series of RSVP drops from $t = 74$ was estimated using the ice-relative measured current velocities at 200 m, kindly provided by R. Muench. One intrusion approximately 50 m high was observed for almost 4 km (Figure 8); however, most of the intrusions were traceable less than 1 km. We caution, however, that much of the variability in the intrusion properties probably occurs in the direction normal to the ISW drift track, since most of the large-scale hydrographic variability is across-slope (see *Muench and Gordon* [this issue, Figure 5]). The observed vertical scales of intrusions, defined as the vertical distance from one temperature maximum to the next, were about 50–100 m. This is consistent with the vertical scale of $O(100)$ m that is obtained from the model of *Toole and Georgi* [1981], using the observed mesoscale horizontal gradient of salinity obtained from the cross-slope CTD transects.

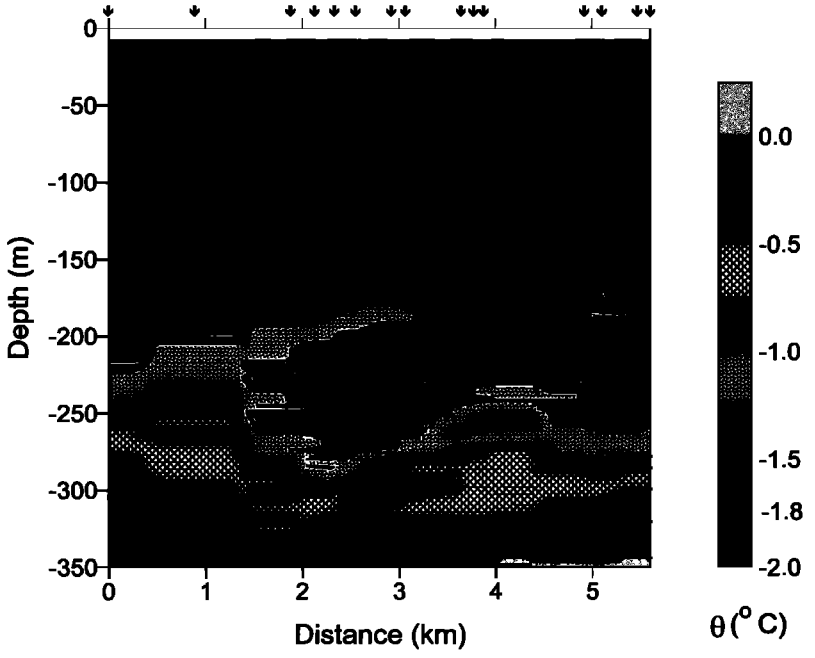

Figure 8. A map of potential temperature, θ, showing the horizontal extent of the intrusions on $t = 74$ using the ice-relative velocity u_{rel} at 200 m to determine distance. Arrows at the top of the plot indicate the locations of the RSVP profiles.

4.2. The Seasonal Pycnocline and the Mixed Layer

The final obstacle to the upward flux of heat from the WDW toward the sea ice is the seasonal pycnocline, which isolates surface effects, such as mixing driven by surface stress and cooling, from the deeper waters of the remnant winter mixed layer. The seasonal pycnocline is located at the base of the surface mixed layer (SML), which is a water layer of nearly constant θ and S in contact with the ice (Figure 3a). In most cases, weak vertical gradients of both θ and S exist in the SML, particularly deeper. For purposes of discussion, we therefore define the lower depth bound of the SML as the depth at which the temperature is 0.04°C greater than θ_{ML}, the average temperature of the upper 20 m. Potential temperature was used rather than density because θ was better resolved in the RSVP data than S. This is a reasonable approach since the seasonal thermocline and halocline coincided during most of the experiment. The mixed layer temperature, θ_{ML}, ranged from -1.85° to -1.89°C during the experiment and was near or slightly above freezing (typically within ~0.02°C, based on the corresponding salinity range of 34.10 to 34.45 psu).

The seasonal pycnocline is visible in transects of both σ_θ (Plate 1c) and buoyancy frequency N (Plate 1d). Values of N in the seasonal pycnocline decreased from greater than 5 cph early in the experiment to less than 3 cph just before it disappeared near $t = 120$. The seasonal pycnocline began to deteriorate significantly around $t = 82$ (Plates 1c and 1d), finally disappearing completely near $t = 120$. Most of the decay occurred during storm events, with about 40% of the total density change across the seasonal pycnocline occurring during the storm event of $t = 86$–91. Another 40% is associated with two other storms (~20% each). Thus 80% of the mixed layer density change was associated with three storm events.

During one storm ($t = 86$–91), *McPhee and Martinson* [1994] used frame-mounted clusters measuring u, v, w, T, and S to obtain direct measurements of the turbulent vertical heat flux $\langle w'T' \rangle$, the covariance of temperature and vertical velocity fluctuations T' and w', respectively, in the upper SML (4–24 m depth). Peak fluxes near 15 W m^{-2} were measured. *McPhee* [1992] found that the turbulent heat flux in the upper mixed layer could be estimated from

$$F_H = \rho\, c_p\, c_H\, u_*\, (T_{ML} - T_f) \qquad (11)$$

where c_H is a constant (~0.005 to 0.006 [*McPhee*, 1992]), T_f is the freezing point temperature for the measured SML salinity, and the friction velocity u_* is determined from

$$u_* = \sqrt{c_{D,25}}\, u_{rel} \qquad (12)$$

In (12), u_{rel} is the measured ice-relative velocity at 25 m, and $c_{D,25}$ is the appropriate ice/water drag coefficient. For rough ice, a reasonable value of $c_{D,25}$ is about 0.005. Using (11) and (12), turbulent heat fluxes (Figure 9) were estimated using T at ~12.5 m depth (the uppermost MDR) for T_{ML} and interpolating S from the LDEO CTD profiles to determine T_f. The highest turbulent heat fluxes occurred during storms, when the ice-relative current speed was greatest. Times of major storms are marked by arrows in Figure 9. The maximum flux of about 15 W m^{-2} for the storm of

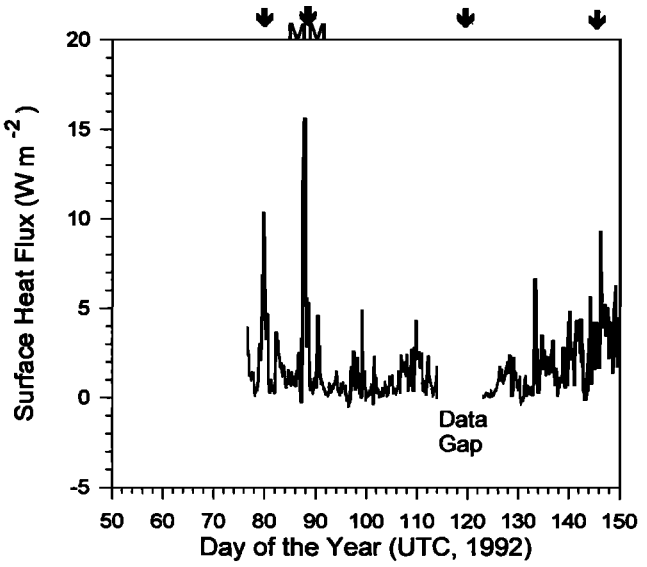

Figure 9. Turbulent heat flux estimates versus time from u_* following *McPhee* [1992]. Times of principal storms are marked with arrows. "MM" denotes the storm of t = 86–91, for which *McPhee and Martinson* [1994] measured a peak turbulent heat flux of 15 W m^{-2}.

t = 86–91 is comparable with the *McPhee and Martinson* [1994] estimate. Between storms, the turbulent heat fluxes were typically less than 2 W m^{-2}. The mean flux for the entire record was 1.7 W m^{-2}. For comparison, V. I. Lytle and S. F. Ackley (Heat flux through sea ice in the western Weddell Sea: Convective and conductive transfer processes, submitted to *Journal of Geophysical Research*, 1995) (hereinafter referred to as Lytle and Ackley, 1995) estimated an average ice flux of 7 W m^{-2} using measurements of ice and snow conditions combined with modeling of the conductive and convective fluxes through the ice and snow cover. While these two estimates disagree, both indicate that the local loss of oceanic heat to the surface is less than the large-scale average of 19 W m^{-2}.

McPhee and Martinson [1994] postulated that the increase in turbulent heat flux due to storms resulted from mixing of the slightly warmer and saltier water of the remnant winter mixed layer into the SML. An example of this mixing can be seen in microscale profiles of θ and velocity shear (u_z) during a storm on day 79 (Figure 10a). The turbulent velocity shear is high throughout the mixed layer. During storm events, surface-generated turbulence frequently extended to the pycnocline (Figure 11). In such cases, mixing entrains water into the mixed layer, thus deepening the SML and at the same time bringing heat and salt upward into the SML [e.g., *McPhee and Martinson*, 1994]. Mixing can also continue across the pycnocline after the surface stress has decreased (Figure 10b). In this case, the source of turbulent kinetic energy is presumably the velocity shear across the seasonal pycnocline, which might be due to mean flow or internal gravity waves.

5. Discussion and Summary

The heat fluxes associated with the various processes described in section 4 are summarized in Figure 12. This figure represents average conditions from late February to late May, 1992 during ISW. About 3 W m^{-2} of upward heat flux occurs in the permanent pycnocline, primarily due to double-diffusive convection. We estimate that 1.7 W m^{-2} finally reaches the base of the pack ice through stress-driven turbulent entrainment of heat from the underlying seasonal pycnocline and remnant winter mixed layer. An additional loss of heat from the warm core occurs through mixing along isopycnals, as suggested by the presence of large intrusions on the inshore side of the warm core. While we are unable to quantify the isopycnal heat flux, we note that the deepest isopycnal for which intrusions are found slopes upward into the surface mixed layer to the east and west of the ISW drift track. Isopycnal mixing therefore provides a plausible mechanism for venting the upper WDW heat to the surface over a broader area than by diapycnal mixing processes alone.

These heat fluxes are significantly less than the 19 W m^{-2} average flux required to explain the overall observed cooling of the water in the Weddell Gyre

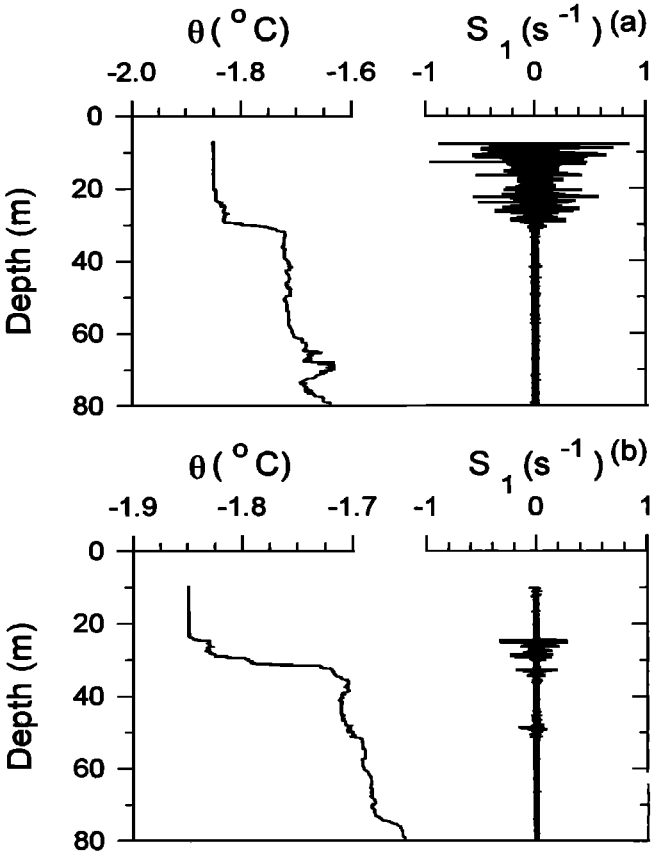

Figure 10. Profiles of potential temperature θ (°C) and one component of velocity shear, S_1, (s^{-1}), (a) at t = 79.701, showing entrainment through the seasonal pycnocline by surface stress and (b) at t = 80.934, showing cross-pycnocline mixing in the absence of surface stress.

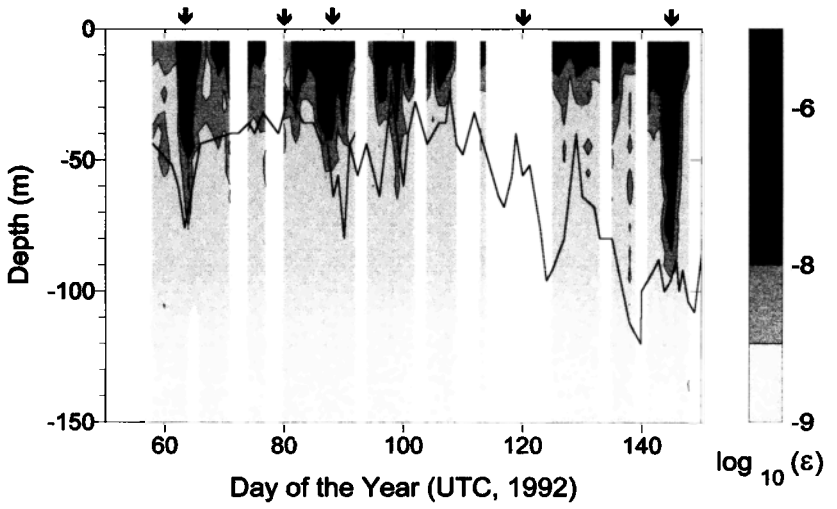

Figure 11. Transects of the mixed layer depth H_{ML} as determined from the LDEO profiles (heavy solid line) and the log of the dissipation rate ε. Times of principal storms are marked with arrows.

[*Fahrbach et al.*, 1994]. This should not be surprising: the thicker second-year ice in this region is a much more efficient insulator between the ocean and atmosphere than the thinner seasonal ice further to the east. In addition the hydrographic and current fields are not amenable to the energetic mixing processes that are possible on the upper slope and shelf. It is, nonetheless, important to understand the heat transport pro-

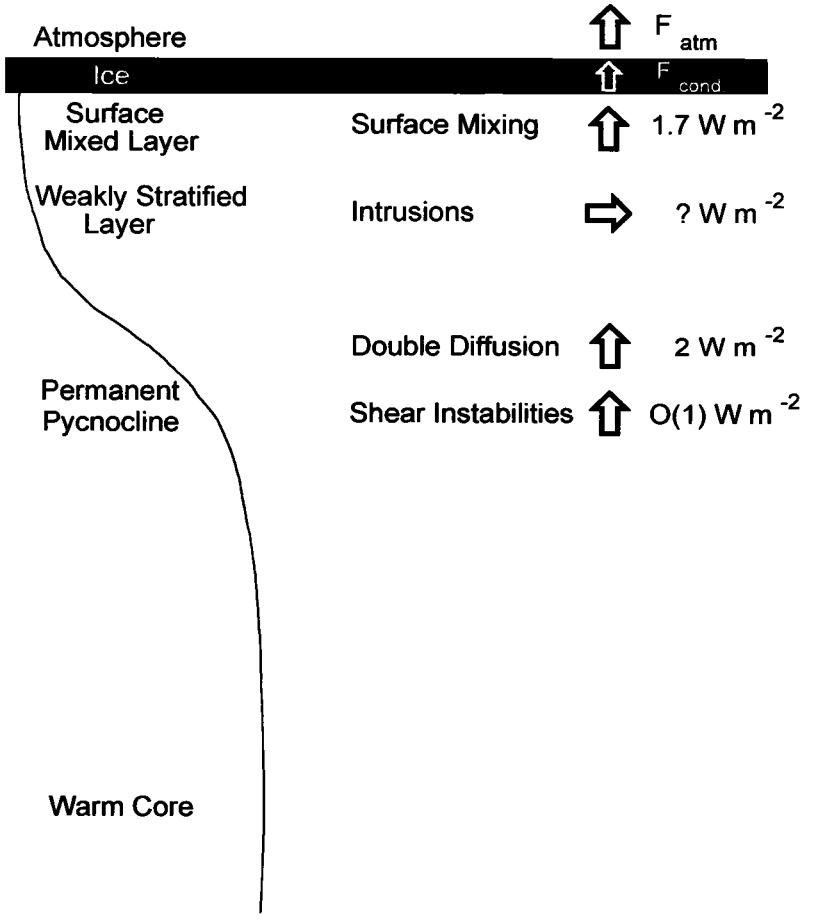

Figure 12. Heat budget for the water column in the western Weddell Sea during ISW. F_{cond} and F_{atm} represent the conductive flux through the ice, and the heat loss to the atmosphere from the snow surface, respectively.

cesses which are present so that the region's sensitivity to perturbations in oceanic and atmospheric conditions can be assessed.

Some support for this inference of low mean fluxes from the ocean to the surface is provided by Lytle and Ackley (submitted manuscript, 1995), who used time series of ice and snow thicknesses and temperatures to model the thermodynamic evolution of the ice at several sites on the ISW floe. They conclude that the mean conductive flux through the ice (denoted F_{cond} on Figure 12) varies between 10 and 30 W m^{-2} during the freeze-up period (days 70 to 92), and between 0 and 15 W m^{-2} during the fall (days 92 to 145). The flux of heat from the snow surface to the atmosphere averaged 9–17 W m^{-2}. For the observed mass balance the required heat flux from the ocean was 7 W m^{-2}, which is significantly larger than our estimate of 1.7 W m^{-2} .

Several processes might contribute to the mismatch between these two estimates of oceanic heat loss to the ice. Since our estimate agrees well with direct measurements of the turbulent flux $\langle w'T' \rangle$ made by *McPhee and Martinson* [1994], we tend to favor the lower value. The complexity of the ice thermodynamics in this region, where much of the new ice formation is via flooding of snow-loaded sea ice rather than growth on the ice base, makes modeling more difficult (Lytle and Ackley, 1995). Significant variability in ice and snow thickness also raises concerns about the applicability of data from the five ice-monitoring sites to the overall transfer of oceanic heat to the sea ice. Nevertheless, both estimates are much lower than the 19 W m^{-2} mean flux required for the Gyre-scale heat budget.

The high dissipation rates that we found at ISW during storms were primarily due to stress-driven mixing caused by the surface-layer water moving relative to the rough ice base. The observed evolution of the SML is not, however, solely due to stress-driven mixing. One possibility is that much of the observed variation in the depth of the SML is due to lateral variability rather than local temporal change. This would not be surprising, given the variability of the mesoscale velocity field as determined from geostrophy by *Muench and Gordon* [this issue]. For example, the strong westward mesoscale flow of about 9 Sv that they find between 67.5° and 68.5°S (t = 101–120) could also advect in the new, deeper surface mixed layer structure that is found subsequent to that time.

The presence of a highly variable mesoscale flow, combined with the sampling constraints imposed by ISW's drift track, precludes simple comparisons between the estimated flux profiles and the observed downstream hydrographic variability of the warm-core current. Some of the hydrographic variability in Figure 4 and Plate 1 is clearly due to the camp's transit over a spatially variable hydrographic field, for example the variation in temperature maxima (T_{max}) between regimes I–II and III–V. Any attempt to explain the apparent downward trend in T_{max} between t = 85 and t = 145 in terms of the observed diapycnal heat fluxes is confused by the addition of fluid to the boundary flow near the Endeavor Ridge [*Muench and Gordon*, this issue].

Considering these caveats our principal conclusions are given below.

1. Double-diffusive convection is the dominant diapycnal heat transport mechanism in the permanent pycnocline, with a maximum estimated upward flux of about 2 W m^{-2} (Figures 6 and 7).

2. Mixing due to shear instabilities in the permanent pycnocline appear to provide a maximum of about 1 W m^{-2} of upward heat flux.

3. Intrusions are frequent in the depth range above the permanent pycnocline. This depth range is associated with isopycnals that intersect the surface mixed layer to the east and west of the ISW drift track. We hypothesize that mixing along these sloping isopycnals could be responsible for further heat loss from the warm core of the boundary current.

4. The seasonal pycnocline, which in summer and early fall protects the remnant of the previous year's winter mixed layer from surface effects, weakens during the ice drift, disappearing entirely near the end of April. The decay is strongly correlated with energetic stress-driven mixing during rapid ice motion in storms, however additional variability may be imposed by mixed-layer lateral advection associated with the mesoscale velocity field described by *Muench and Gordon* [this issue].

5. The mean heat loss from the ocean to the ice is about 1.7 W m^{-2}.

Ice Station Weddell was the first oceanographic study in the western Weddell Sea to obtain modern finescale and microscale measurements that allow direct estimates of fluxes in this region. Further measurements would be necessary to fully understand the small-scale mixing processes in the various hydrographic and current regimes revealed by the concurrent large-scale surveys described by *Muench and Gordon* [this issue]. In many ways, the warm core current that was under ISW for most of the experiment is an anomalous component of the general northward flow of the western Weddell Gyre, which includes the shelf circulation to the west and the more horizontally homogeneous hydrography of the central Gyre to the east of the ISW drift track. Mixing mechanisms over the upper slope and broad continental shelf [e.g., *Carmack*, 1986] differ significantly from those revealed by the present study. From data collected in the southern Weddell Sea, *Foster et al.* [1987] proposed that barotropic shelf waves could advect the WDW, which is generally confined seaward of the shelf/slope front, onto the shelf where mixing could be accomplished by shear instabilities in the semidiurnal tides and perhaps higher-frequency internal gravity waves. Nonlinearities in the equation of state, such as cabbeling [*Fofonoff*, 1956; *Foster*, 1972; *Foster and Carmack*, 1976a] and thermobaricity [*Gill*, 1973] also become critical as the density contrast between surface and deeper waters is reduced. Similar processes are presumably operating over the shelf and slope in

the western Weddell Sea, since the cross-slope hydrographic structure [see *Muench and Gordon*, this issue] is similar to the southern shelf/slope. It is suggested that future studies in this region concentrate on mixing processes over the upper slope and central shelf, in particular the interaction between shelf water and WDW at the shelf/slope front.

Acknowledgments. This study was supported by NSF, contracts DPP-9024695 and OPP-9317319. We gratefully acknowledge the scientific leadership of A. Gordon, and logistics support of J. Ardai, Antarctic Support Associates, and the Russian Arctic and Antarctic Research Institute. We are indebted to D. Martinson and T. Baker (LDEO) for continuing the micro-structure profiling through the final two legs of ISW. CTD data were kindly provided by A. Gordon, and current meter data were provided by R. Muench. We also thank R. Muench, M. McPhee, D. Kelley, V. Lytle, S. Ackley, and an anonymous reviewer for their critical comments on the draft manuscript.

References

Baker, M. A., and C. H. Gibson, Sampling turbulence in the stratified ocean: Statistical consequences of strong interactions, *J. Phys. Oceanogr., 17,* 1817–1836, 1987.

Bathmann, U., V. Smetacek, H. de Baar, E. Fahrbach, and G. Krause, The expeditions ANTARKTIS X/6-8 of the research vessel "*Polarstern*" in 1992/93, *Rep. Polar Res. 135,* Alfred-Wegener Inst. for Polar and Mar. Res., Germany, 1994.

Boyd, T. J., and E. A. D'Asaro, Cooling of the West Spitsbergen Current, *J. Geophys. Res., 99,* 22,597–22,618, 1994.

Caldwell, D. R., T. M. Dillon, and J. N. Moum, The rapid-sampling vertical profiler: An evaluation, *J. Atmos. Oceanic Technol., 2,* 615–625, 1985.

Carmack, E. C., Circulation and mixing in ice-covered waters, in *The Geophysics of Sea Ice,* edited by N. Untersteiner, pp. 641–712, Plenum, New York, 1986.

Dillon, T. M., The energetics of overturning structures: Implications for the theory of fossil turbulence, *J. Phys. Oceanogr., 14,* 541–549, 1984.

Fahrbach, E., G. Rohardt, M. Schröder, and V. Strass, Transport and structure of the Weddell Gyre, *Ann. Geophys., 12,* 840–855, 1994.

Fernando, H. J. S., Oceanographic implications of laboratory experiments on diffusive interfaces, *J. Phys. Oceanogr., 19,* 1707–1715, 1989.

Fofonoff, N. P., Some properties of sea water influencing the formation of Antarctic bottom water, *Deep Sea Res., 4,* 32–35, 1956.

Foster, T. D., An analysis of the cabbeling instability in sea water, *J. Phys. Oceanogr., 2,* 294–301, 1972.

Foster, T. D., and E. C. Carmack, Temperature and salinity structure in the Weddell Sea, *J. Phys. Oceanogr., 6,* 36–44, 1976a.

Foster, T. D., and E. C. Carmack, Frontal zone mixing and Antarctic Bottom Water formation in the southern Weddell Sea, *Deep Sea Res., 23,* 301–317, 1976b.

Foster, T. D., A. Foldvik, and J. H. Middleton, Mixing and bottom water formation in the shelf break region of the southern Weddell Sea, *Deep Sea Res., 34,* 1771–1794, 1987.

Gill, A. E., Circulation and bottom water production in the Weddell Sea, *Deep Sea Res., 20,* 111–140, 1973.

Gordon, A. L., and B. A. Huber, Southern Ocean winter mixed layer, *J. Geophys. Res., 95,* 11,655–11,672, 1990.

Gordon, A. L., B. A. Huber, H. H. Hellmer, and A. Ffield, Deep and bottom water of the Weddell Sea's western rim, *Science, 262,* 95–97, 1993a.

Gordon, A. L., and Ice Station Weddell Group of Principal Investigators and Chief Scientists, Weddell Sea exploration from ice station, *Eos Trans. AGU, 74,* 121–126, 1993b.

Gregg, M.C., Diapycnal mixing in the thermocline: A review, *J. Geophys. Res., 94,* 5249–5286, 1987.

Gregg, M. C., Scaling turbulent dissipation in the thermocline, *J. Geophys. Res., 94,* 9686–9698, 1989.

Huber, B. A., P. A. Mele, W. E. Haines, A. L. Gordon, and V. I. Lukin, Ice Station Weddell, 1, CTD/Hydrographic Data, *Tech. Rep. LDEO-94-2,* Lamont-Doherty Geol. Obs., Palisades, N.Y., 1994.

Kelley, D., Effective diffusivities within thermohaline staircases, *J. Geophys. Res., 89,* 10,484–10,488, 1984.

Kelley, D., Fluxes through diffusive staircases: A new formulation, *J. Geophys. Res., 95,* 3365–3371, 1990.

LaBreque, J. L., and M. E. Ghidella, Estimates of bathymetry, depth to magnetic basement, and sediment thickness for the western Weddell Basin, *Antarc. J. U.S., 27,* 68–70, 1993.

Ledwell, J. R., A. J. Watson, and C. S. Law, Evidence for slow mixing across the pycnocline from an open-ocean tracer-release experiment, *Nature, 364,* 701–703, 1993.

Marmorino, G. O., and D. R. Caldwell, Heat and salt transport through a diffusive thermohaline interface, *Deep Sea Res., 23,* 59–67, 1976.

McPhee, M. G., Analysis and prediction of short-term ice drift, *J. Offshore Mech. Arct. Eng., 110,* 94–100, 1988.

McPhee, M. G., Turbulent heat flux in the upper ocean under sea ice, *J. Geophys. Res., 97,* 5365–5379, 1992.

McPhee, M. G., On the turbulent mixing length in the oceanic boundary layer, *J. Phys. Oceanogr., 24,* 2014–2031, 1994.

McPhee, M. G., and D. G. Martinson, Turbulent mixing under drifting pack ice in the Weddell Sea, *Science, 263,* 219–220, 1994.

Muench, R. D., and A. L. Gordon, Circulation and transport of water along the western Weddell Sea margin, *J. Geophys. Res.,* this issue.

Muench, R. D., H. J. S. Fernando, and G. R. Stegen, Temperature and salinity staircases in the northwestern Weddell Sea, *J. Phys. Oceanogr., 20,* 295–306, 1990.

Muench, R. D., M. D. Morehead, and J. T. Gunn, Regional current measurements in the western Weddell Sea, *Antarc. J. U.S., 27,* 108, 1993.

Orsi, A. H., W. D. Nowlin, Jr., and T. Whitworth III, On the circulation and stratification of the Weddell Gyre, *Deep Sea Res., 40,* 169–203, 1993.

Osborn, T. R., Estimates of the local rate of vertical diffusion from dissipation measurements, *J. Phys. Oceanogr., 10,* 83–89, 1980.

Osborn, T. R., and W. R. Crawford, An airfoil probe for measuring turbulent velocity fluctuations in water, in *Air-Sea Interactions: Instruments and Methods,* pp. 369–386, Plenum, New York, 1980.

Padman, L., Small-scale physical processes in the Arctic Ocean, in *Arctic Oceanography: Marginal Ice Zones and Continental Shelves, Coastal Estuarine Stud.,* vol.49, edited by W.O. Smith and J. M. Grebmeier, pp. 97-129, AGU, Washington, D.C., 1995.

Padman, L., and T. M. Dillon, Vertical heat fluxes through the Beaufort Sea thermohaline staircase, *J. Geophys. Res., 92,* 10,799–10,806, 1987.

Padman, L., and T. M. Dillon, On the horizontal extent of

the Canada Basin thermohaline steps, *J. Phys. Oceanogr., 18,* 1458–1462, 1988.

Padman, L., and T. M. Dillon, Turbulent mixing near the Yermak Plateau during the Coordinated Eastern Arctic Experiment, *J. Geophys. Res., 96,* 4769–4782, 1991.

Ruddick, B., A practical indicator of the stability of the water column to double-diffusive activity, *Deep Sea Res., 30,* 1105–1107, 1983.

Ruddick, B., and D. Walsh, Observations of the density perturbations which drive thermohaline intrusions, in *Proceedings of the Chapman Conference on Double-Diffusive Convection,* Scottsdale, AZ, 1995.

Rudels, B., The diffusive interface at low stability: The importance of non-linearity and turbulent entrainment, *Tellus Series A, 43,* 153–167, 1991.

Schmitt, R. W., Double diffusion in oceanography, *Ann. Rev. Fluid Mech., 26,* 255–285, 1994.

Stillinger, D. C., K. N. Helland, and C. W. Van Atta, Experiments of the transition of homogeneous turbulence to internal waves in a stratified fluid, *J. Fluid Mech., 131,* 91–122, 1983.

Taylor, J., The fluxes across a diffusive interface at low values of the density ratio, *Deep Sea Res., 35,* 555–567, 1988.

Tennekes, H., and J. L. Lumley, *A First Course in Turbulence,* 300 pp., MIT Press, Cambridge, Mass., 1992.

Toole, J. M., and D. T. Georgi, On the dynamics and effects of double-diffusively driven intrusions, *Prog. Oceanogr., 10,* 123–145, 1981.

Turner, J. S., *Buoyancy Effects in Fluids,* 368 pp., Cambridge Univ. Press, New York, 1973.

Walsh, D., and B. Ruddick, Double-diffusive interleaving: The influence of non-constant diffusivities, *J. Phys. Oceanogr., 25,* 348–358, 1995.

Wijesekera, H. W., L. Padman, T. M. Dillon, M. D. Levine, C. A. Paulson, and R. Pinkel, The application of internal wave dissipation models to a region of strong mixing, *J. Phys. Oceanogr., 23,* 269–286, 1993.

M. D. Levine, L. Padman, and R. Robertson, College of Oceanic and Atmospheric Sciences, Oregon State University, Oceanography Administration Building 104, Corvallis, OR 97331-5503.

(Received December 1, 1994; revised May 31, 1995; accepted June 5, 1995.)